

Received 21 March 2014; revised 7 May 2014 and 28 June 2014; accepted 30 July 2014. Date of current version 22 April 2015.  
The review of this paper was arranged by Editor R. Singh.

Digital Object Identifier 10.1109/JEDS.2014.2345556

# CuIn<sub>1-x</sub>Al<sub>x</sub>Se<sub>2</sub> Thin Films Grown by Co-Sputtering and Modified Selenization: Application in Flexible Solar Cells

MURALI BANAVOTH, M. MADHURI, AND S. B. KRUPANIDHI

Materials Research Centre, Indian Institute of Science, Bangalore 560012, India

CORRESPONDING AUTHOR: S. B. KRUPANIDHI (e-mail: sbk@mrc.iisc.ernet.in)

**ABSTRACT** Thin films of CuIn<sub>1-x</sub>Al<sub>x</sub>Se<sub>2</sub> (CIAS) were grown on the flexible 10 micrometer thin stainless steel substrates, by dc co-sputtering from the elemental cathodes, followed by annealing with modified selenization. CuInAl alloyed precursor films were selenized both by noble gas assisted Se vapor transport in a tubular furnace and vacuum evaporation of Se in an evaporation chamber. CIAS thin films were optimized for better adhesion. X-ray diffraction, scanning electron microscopy, and UV-visible absorption spectroscopy were used to characterize the selenized films. The composition of CIAS films was varied by substituting In with Al in CuInSe<sub>2</sub> (CIS) from  $0 \leq x \leq 0.65$  ( $x = \text{Al}/(\text{Al}+\text{In})$ ). Lattice parameters, average crystallite sizes, and compact density of the films, decreased when compared to CIS and (112) peak shifted to higher Bragg's angle, upon Al incorporation. The dislocation density and strain were found to increase with Al doping. Solar cells with SS/Mo/CIAS/CdS/iZnO:AZnO/Al configuration were fabricated and were tested for current-voltage characteristics for various 'x' values, under Air Mass 1.5 Global one sun illumination. The best CIAS solar cell showed the efficiency of 6.8%, with  $x = 0.13$ ,  $E_g = 1.17$  eV, fill factor 45.04, and short circuit current density  $J_{sc}$  30 mA/cm<sup>2</sup>.

**INDEX TERMS** Inorganic materials, instruments, photovoltaic cells, sputtering, thin films.

## I. INTRODUCTION

Recently much of the research interest has been devoted to polycrystalline CIS (CuInSe<sub>2</sub>) based alloyed solar cells. CIS being the lowest member of Cu-chalcopyrite group and a ternary semiconductor with a direct band gap of 1.0 eV, an absorption coefficient of  $3.6 \times 10^5$  cm<sup>-1</sup> [1], [2] has reached 14.6% record conversion efficiency for the device fabricated on soda lime glass (SLG) in SLG/Mo/CIS/CdS/i-ZnO:AZnO/Al configuration. Band gap of CIS can be tuned by doping group III elements, for instance Ga or Al. The band gap of CuIn<sub>1-x</sub>Ga<sub>x</sub>Se<sub>2</sub> (CIGS) can be tailored from 1.0 to 1.7 eV by varying the  $x = \text{Ga}/(\text{Ga}+\text{In})$  ratio from 0 to unity. CIGS has reached the maximum efficiency [3] of 20.1% with  $x = 0.3$  and  $E_g = 1.15$  eV and was found to limit the efficiency for  $x = 0.5$  and  $E_g = 1.3$  eV. The limitation to the efficiency upon excess Ga doping could be due to the increase in the defect concentration and thereby leading to the recombination [4].

CuIn<sub>1-x</sub>Al<sub>x</sub>Se<sub>2</sub> (CIAS), where  $x = \text{Al}/(\text{Al}+\text{In})$ , being an alternative wide band gap material, is formed by replacing indium with aluminum. Till date a record efficiency of 16.9% has been obtained using a co-evaporation process [5]. Band gap can be varied from ~1 eV (CuInSe<sub>2</sub>) to ~2.7 eV (CuAlSe<sub>2</sub>). Noteworthy that low Al alloying would compensate the higher Ga alloying, for achieving higher band gap. Besides higher Ga doping would incorporate significant structural changes compared to that of Al doping [6]. Hence CIAS based solar cells are currently focused upon [7]. CIAS absorber films were deposited by co-sputtering which allowed scaling up at the larger modules with better compositional uniformity. CIA alloys were selenized in the selenium atmosphere involving Se vapor transport in a tubular furnace and evaporation of Se in an evaporation chamber. Selenization of the CIA films required proper control over selenium [8] for avoiding the adhesion issues with respect to back contact and crystallinity of the selenized films.

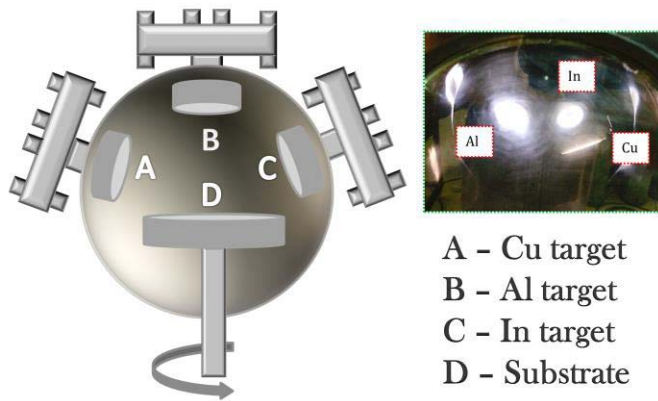


**FIGURE 1.** Schematic dc-sputtering used for CIA alloy deposition (inset showing the plasma of elemental cathodes).

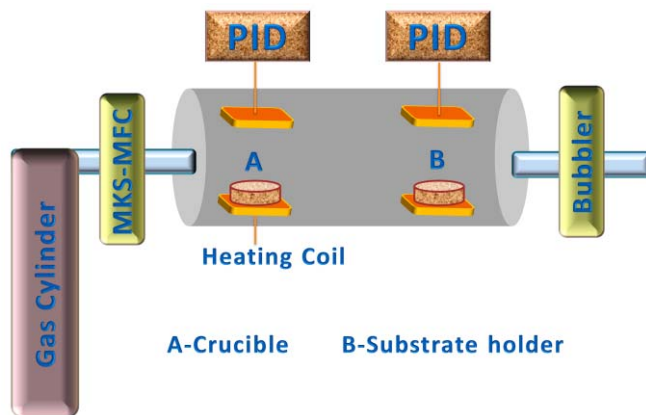


**FIGURE 2.** Schematic set up used for selenization of co-sputtered CuInAl alloyed thin films.

Flexible solar cells are desirable due to its low weight, low cost, longer life times upon encapsulation and flexibility in roll-to-roll manufacturing [9]. The space and building applications of solar cells, find effective utilization of flexible substrates. Polyamide substrates are the strong candidates for their flexibility [10]. CIAS absorber phase optimization involved the annealing at 450 °C for which the polyamide sheets would not withstand such a high temperature. Hence the stainless steel substrates have attracted great attention for space applications. Nevertheless the stainless steel substrates used for solar cells should satisfy the following criteria for avoiding the efficiency losses [11], [12]: a) matching of thermal coefficient of expansion for better adhesion of CIAS films, b) Higher chemical stability in all environmental conditions, c) Substrate degassing should be minimized, d) Carbon content in the steel should be minimum, e) Corrosion resistant steel foils are desirable, f) Enamel coatings should withstand higher temperatures, in Se atmosphere, g) Absorber doping is allowed through enamel on steel substrates.

In this enhanced article of our previous paper [13], current work extends the range of knowledge in understanding

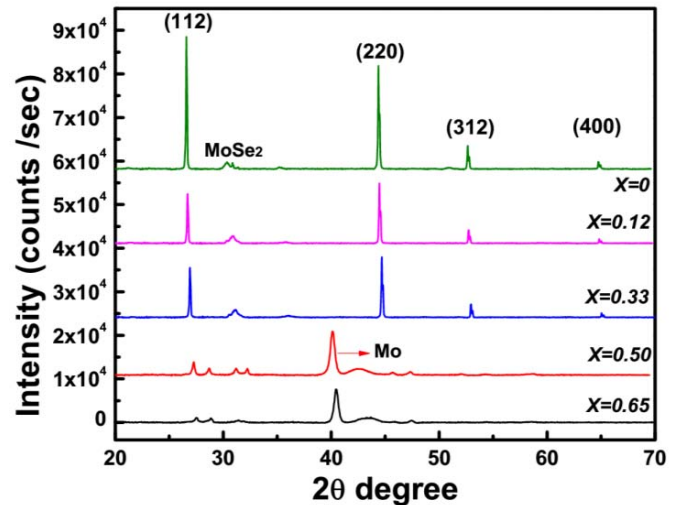


**FIGURE 3.** X-ray diffraction of CIAS thin films.

the texture, strain, lattice parameters and current-voltage characteristics of solar cells fabricated on stainless steel substrates, as a function of Al doping. The intentional Al doping in the CIS absorber leads to the structural changes and hence band gap gets modulated, which shows detrimental effects on the device electrical and electronic properties. Conventional thin film chalcopyrite solar cell fabrication involves the usage of 3-5 mm thick soda lime glass substrates which limits its space and terrestrial applications. Hence thin metallic/polymer foils of 5-50 μm thickness are advantageous, in terms of weight and flexibility of wrapping around any curved surfaces [14]. Thin stainless steel foils of 10 micron were successfully used for fabrication of the complete solar cells with in SS/Mo/CIAS/CdS/i-ZnO-AZnO/Al configuration. Effects of the Al doping upon the grain sizes were correlated with XRD and SEM.

## II. EXPERIMENT

CIA metallic films were co-sputtered from the three single elemental cathodes, which are con-focally arranged towards the 6" rotating substrate holder. The elemental cathodes were operated under direct current (dc) power supply. Dc-magnetron sputtering chamber was equipped with a 3" Mo cathode, procured from Kurtz J Leskar, which was used for depositing a uniform Mo film of desired thickness. Firstly, Mo was pre-sputtered to ensure a clean surface and devoid of any contaminants in the sputtering chamber. Sputtering chamber (Fig. 1) was evacuated to  $5 \times 10^{-7}$  mbar, followed by 4 sccm argon purging to maintain a constant  $2 \times 10^{-3}$  mbar working pressure throughout the deposition. The uniformity of the thin film deposition was ensured by rotating the substrate assembly at 30 rpm, during the entire co-sputtering process. Initially CuIn (CI) alloy was deposited for 10 minutes, followed by CIA alloy and finally depositing 200 nm Cu cap to prevent the indium aggregation and Al<sub>2</sub>O<sub>3</sub> formation at the top surface. The time intervals of Al and In

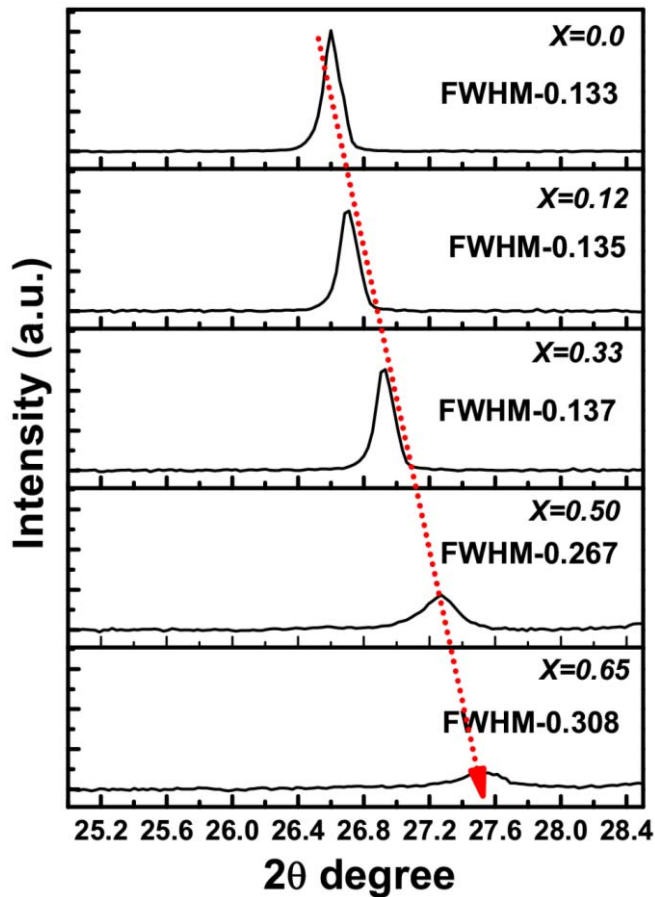


**FIGURE 4.** Full width at half maximum in CIAS thin films as a function of 'x' for various compositions.

were varied to yield different 'x' ratios. The power density ( $W/cm^2$ ) of the Al and In guns were adjusted to fine tune the desired thin film compositions. Six batches of the CIA films were deposited by varying the Al compositions. Films were deposited both on the SLG substrates and flexible stainless steel ( $10\ \mu m$  thick) substrates. Structural analyses of CIAS absorber were carried out on the SLG/CIAS thin films.

#### A. SELENIZATION OF THE CIA PRECURSOR FILMS

Selenization was performed in two different ways 1) Thermal evaporation of elemental selenium by means of resistive heating and monitoring the deposition using a quartz crystal monitor. Selenization was performed in a Hi pace 300 turbo-pumped thermal evaporation chamber under a base pressure of  $\sim 1 \times 10^{-6}$  m bar with substrate assembly maintained at  $450^\circ C$ . The deposition rate was monitored through closed-loop feedback with a quartz crystal monitor. 2) Tubular furnace equipped with a thermocouple was positioned at one end of the furnace, for measuring the temperature of the crucible containing selenium granules. CIA films annealed in open air by a conventional tubular furnace, contained the oxide impurities of Cu, In and Al, as evidenced from the XRD data. Hence a modified annealing route was employed,

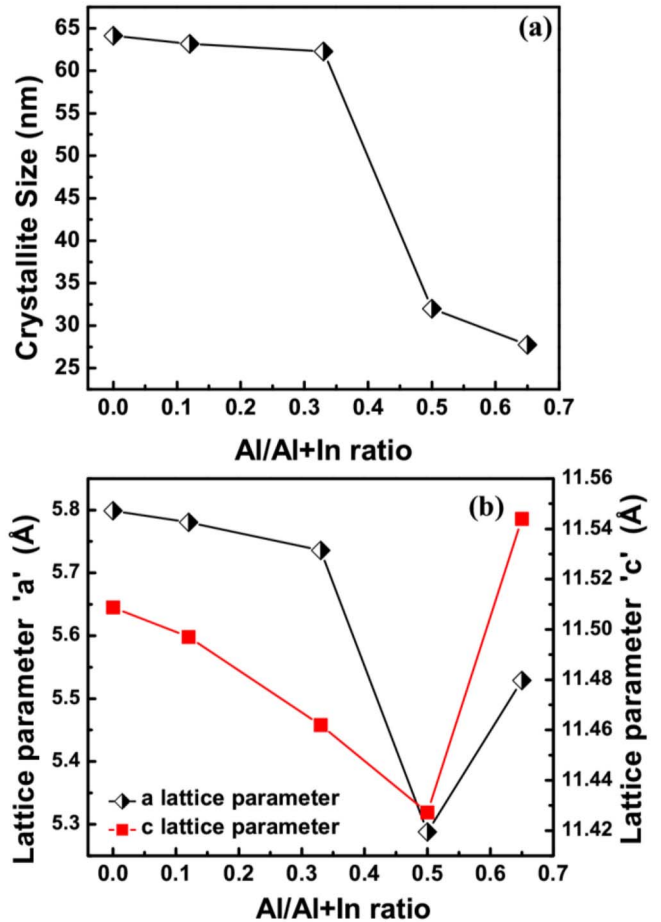


**FIGURE 5.** (a) Crystallite size distribution and (b) lattice parameter variation in the CIAS thin films function of 'x' for various compositions.

in which the noble gas mixture (Ar: He) was purged from one end for 5 minutes and other end closed with a bubbler in order to monitor the gas flowing out. Such a set up ensures the absence of oxygen inside the furnace. Then the heating profile of the selenium was started by, flowing the noble gas at 1 sccm, monitored by a MKS gas mass flow controller. The heating profile of the CIA alloy films was started simultaneously at a ramping rate of  $8^\circ C/min$ . Better crystallinity and control over the selenium content was obtained in the case of annealing in the modified tubular furnace as depicted from the XRD graphs.

Initially the samples were selenized at a flux rate of  $10\ \text{Å/S}$ , in the turbo-connected thermal evaporation chamber, for about 30 minutes. The samples were found to be selenium deficient and then the annealing time was increased to 45 minutes, maintaining the substrate temperature at  $500^\circ C$ , where the samples contained 50 % selenium.

Second process of annealing, was performed in a modified tubular furnace (Fig. 2) by maintaining the crucible temperature at  $230^\circ C$  with a ramp rate of  $3^\circ C/min$  and the substrate holder at  $500^\circ C$  with a ramp rate of  $8^\circ C/min$  respectively. When the samples were placed at the center of the furnace with a single heating coil at the center, films were peeled

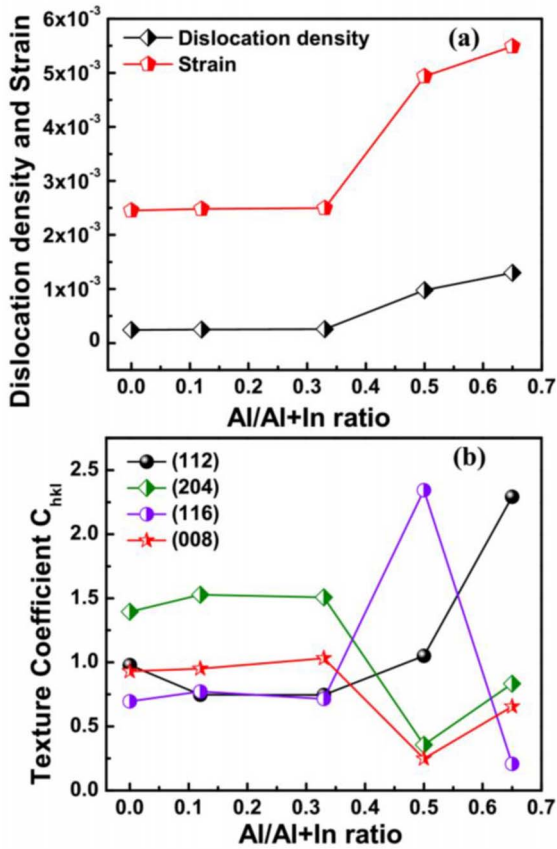


**FIGURE 6.** (a) Dislocation density and strain. (b) Texture coefficient of CIAS films grown on SS/Mo as a function of 'x' for various compositions.

off or the films were poorly adhered. Once the modified set was used, films with good adhesion were obtained. Selenium was found to be deficient in the case of 60 min annealing and up on prolonging to 90 min, stoichiometric films were obtained.

## B. CHARACTERIZATION TECHNIQUES

Bruker D8 advance X-ray powder diffractometer, with monochromatic Cu K $\alpha$  radiation ( $\lambda = 1.5406 \text{ \AA}$ ) was used to record the X-ray diffraction pattern for phase identification. The morphology of the CIA and CIAS thin films were investigated by field emission scanning electron microscope (Zeiss Gemini FESEM). Perkin Elmer UV-VIS-NIR spectrometer was used to record the transmittance spectrum of selenized films. A.M 1.5 G simulated solar Simulator, Oriol Sol 3A with KG5 filtered lamp source, NREL calibrated Si reference cell (oriol P/N-91150V) to 100 mW/cm<sup>2</sup>) equipped with 2400 Keithley source measurement unit.

## C. PHASE IDENTIFICATION

X-ray diffraction pattern (Fig. 3) was indexed to the standard JCPDS Pdf file No. 40-1487 of CuInSe<sub>2</sub>, with the lattice constants  $a = 5.12 \text{ \AA}$ ,  $c = 11.27 \text{ \AA}$ . Absence of secondary phases pertaining to CuS, In<sub>2</sub>S<sub>3</sub> etc confirmed the phase purity and complete selenization of the CuInAl alloyed thin films. Al compositions with  $x = 0, 0.12$  &  $0.33$  set of films were

selenized in the modified set up and the  $x = 0.50$  &  $0.65$  set of films were selenized in the thermal evaporation. It was observed that the crystallinity was better in case of films annealed in the modified set up. Fig. 4 showed the variation of full width at half maximum with respect to the Al doping. Upon increase in the 'x' for various compositions, the FWHM of the CIAS thin films on SS/Mo substrate, increased with shift in the (112) peak towards the higher angles. A shift from  $2\theta$  values 26.6 at  $x = 0$  to 27.5 at  $x = 0.65$  was observed. Such a shift in the (112) peak, could be attributed to the lattice spacing shrinking of (112) orientation as per Vegard's law. It is to be noted that the higher angle shifting of the peaks could also be due to the intrinsic strain release in the film. The crystallite sizes of CIAS films were estimated from the Scherrer relation [15]. Where  $D$  is the grain size of crystallite,  $\lambda$  ( $1.5405 \text{ \AA}$ ) the wavelength of X-rays used,  $\beta$  being the half its maximum intensity in radians and  $\theta$  is the angle of diffraction.

$$D = \frac{0.9\lambda}{\beta \cos\theta} \quad (1)$$

Lattice parameters were calculated using the relation (2).

$$\frac{1}{d^2} = \frac{h^2 + k^2}{a^2} + \frac{l^2}{c^2} \quad (2)$$

Where  $d$  is the  $d$  spacing,  $h, k, l$  are miller indices and 'a', 'c' are the lattice constants.

Fig. 5(a) showed the decrease in the crystallite sizes with Al doping composition. Fig. 5(b) showed that the lattice parameter 'a' decreased with Al doping into CIS films, indicating the shrinkage in the lattice, further confirming the possibility of (112) peak shift. The doping atoms in general might form solid solutions with different mechanisms [16]. A situation when  $X = 0.5$  is the case where the doping atom Al<sup>3+</sup> substitute the matrix atoms in order to form a lattice, so the final lattice parameter was decreased. In another case, when  $x \geq 0.65$  the doping atom enters the interstitial space forming the interstitial solutions, hence the lattice parameter was increased since the lattice was distorted and expanded by the doping atoms. Strain and dislocation density [Fig. 6(a)] were calculated using the eqn. 3 and 4 respectively [17] and were found to increase with percentage doping of Al in CIS crystal lattice. It is to be noted that the strain incorporated into the films could possibly be due to the imperfections in the crystal lattice. Such imperfections arise due to the stacking faults, vacancies and interstitials etc. In order to quantify the orientation of a particular plane, texture coefficients (TC<sub>hkl</sub>) were calculated [18] (eqn. 5).

$$\rho = \frac{1}{D^2} \quad (3)$$

$$\varepsilon = \frac{\beta}{4 \tan\theta} \quad (4)$$

Where  $\varepsilon$  the strain and  $\beta$  is full width at half maximum.

$$TC_{hkl} = \frac{\frac{I_{(hkl)}}{I_{o(h'k'l')}}}{\frac{1}{N} \sum \frac{I_{(hkl)}}{I_{o(h'k'l')}}} \quad (5)$$

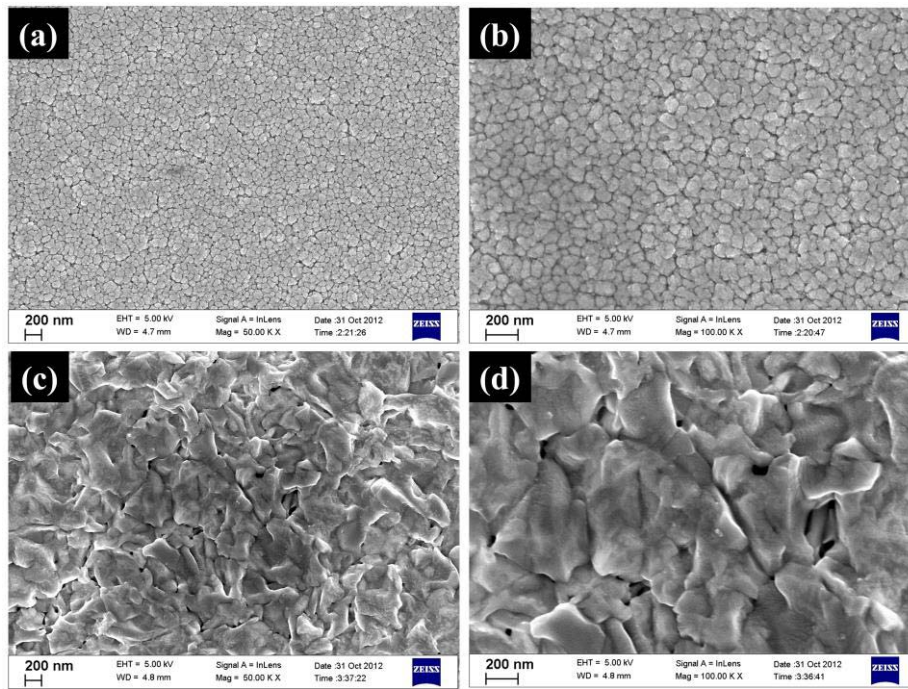


**FIGURE 7.** SEM images of (a) and (b) co-sputtered CIA alloyed thin films, (c) and (d) selenized CIAS thin films with  $x = 0$  at different magnifications.

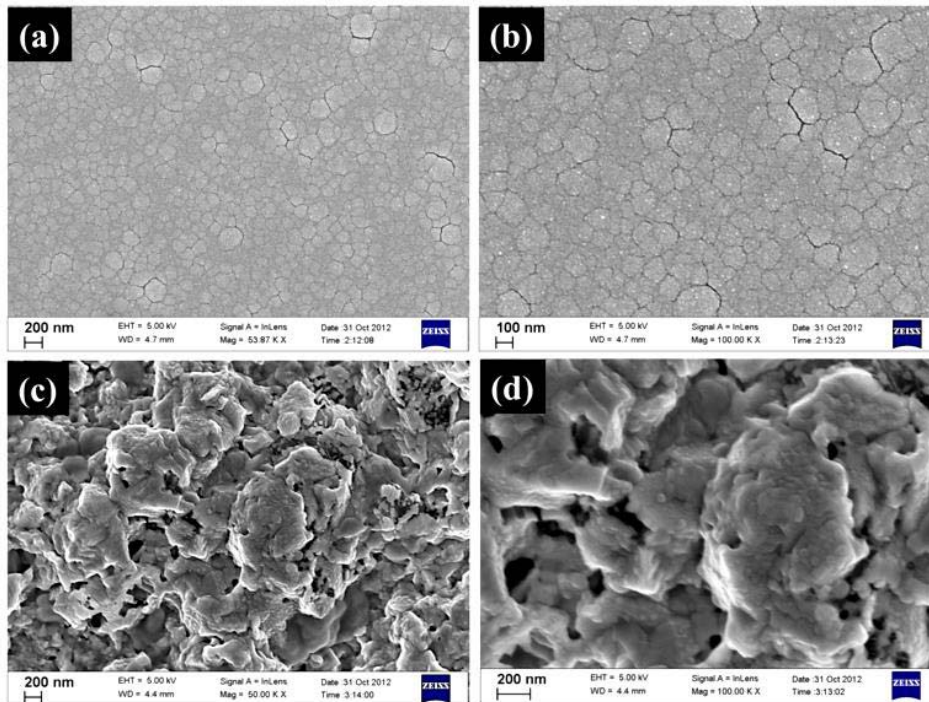
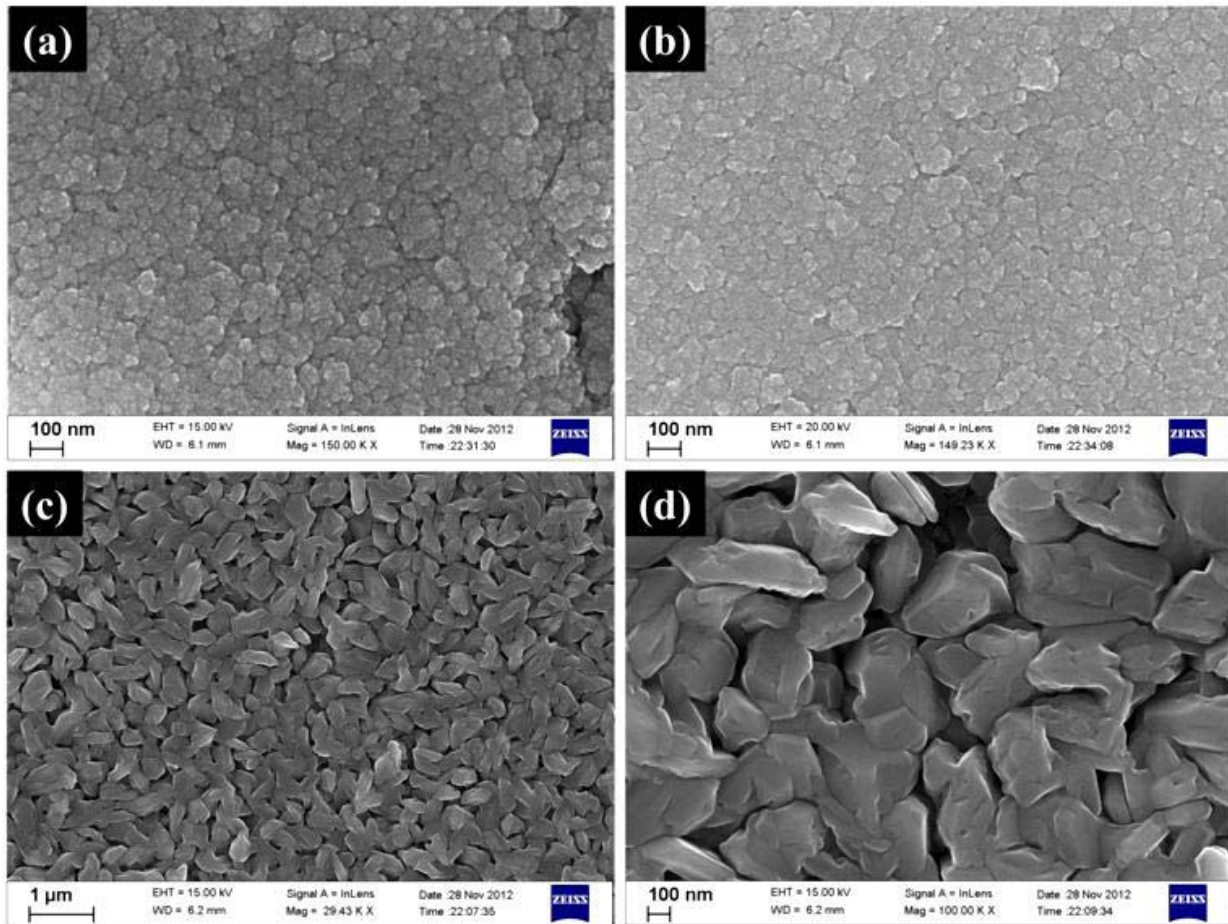


**FIGURE 8.** SEM images of (a) and (b) co-sputtered CIA alloyed thin films, (c) and (d) selenized CIAS thin films with  $x = 0.13$  at different magnifications.

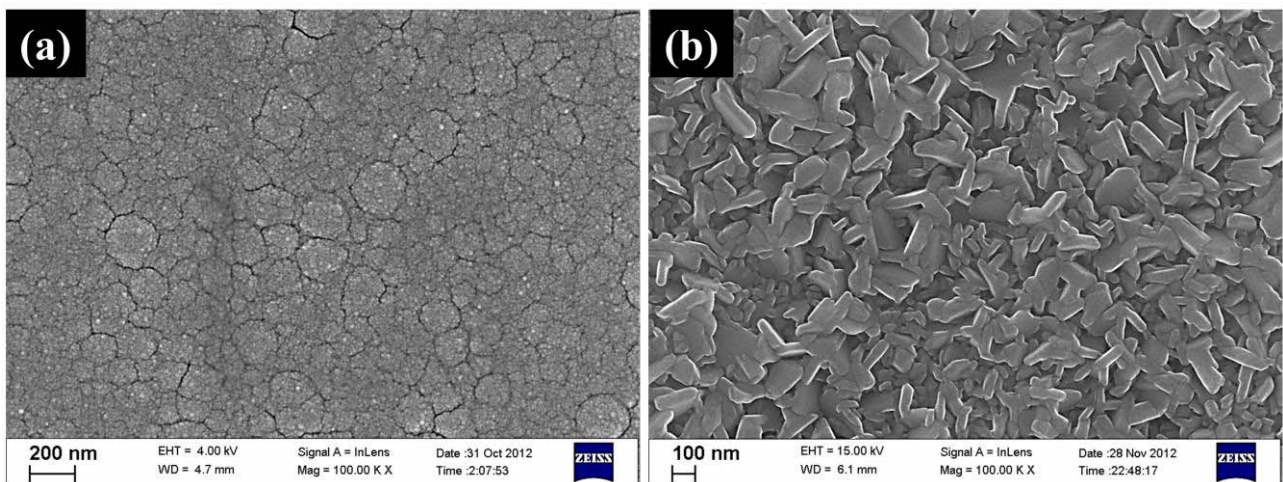
Where  $I_{hkl}$  is the obtained intensity of the (hkl) diffraction peak and  $I_{h'k'l'}$  is the relative intensity of JCPDS standard data.  $N$  is the number of reflections considered.

Fig. 6(b) showed the TC values for different Al compositions as a function of Bragg planes. Bragg plane (204)

showed higher TC value than the strong reflection (112) in case of  $x = 0, 0.12, 0.33$ , whereas for  $x = 0.5$  the plane (116) showed higher value and (112) for  $x = 0.65$ . In general such deviations could be due to the increase in the structural factor or induced lattice deformation [17].



**FIGURE 9.** SEM images of (a) and (b) co-sputtered CIA alloyed thin films, (c) and (d) selenized CIAS thin films with  $x = 0.5$  at different magnifications.



**FIGURE 10.** SEM images of (a) co-sputtered CIA alloyed thin films, (b) selenized CIAS thin films with  $x = 0.65$  at different magnifications.

#### **D. MORPHOLOGICAL INVESTIGATIONS**

Scanning electron micro graphs of the both CIA alloyed films and CIAS films at various magnifications with varying compositions of ' $x$ ' were presented in the Figs. 7–10. CIA alloyed precursor thin films showed almost similar

grain growth whereas the CIAS films showed different morphologies. Grain sizes of the CIAS films decreased with increase in ' $x$ ' ratio [19]. The grain sizes obtained from SEM images were in agreement with those obtained from XRD calculations.

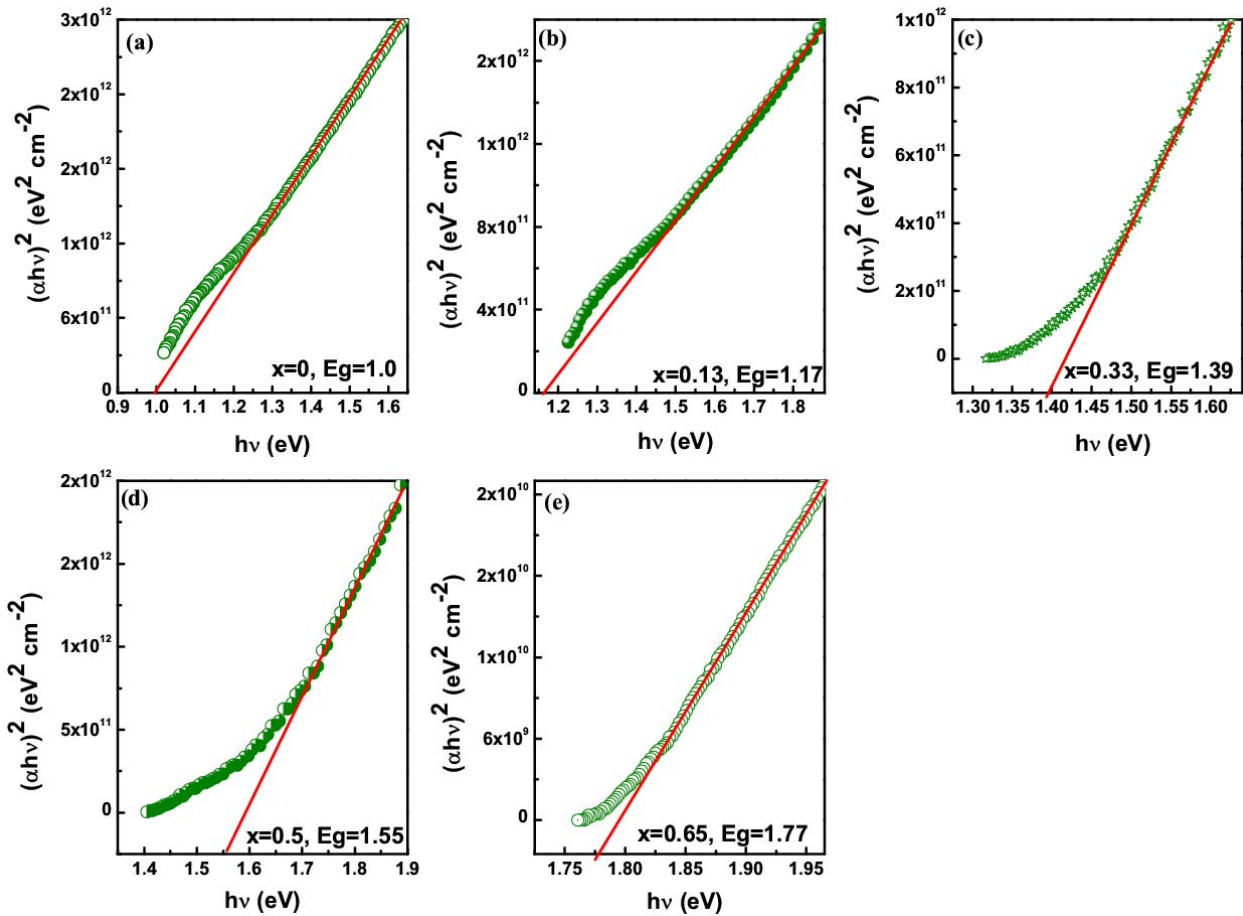


**FIGURE 11.** Band gap calculated for different 'x' ratios of CIAS thin films. (a)  $E_g = 1.0$  for  $x = 0$ . (b)  $E_g = 1.17$  for  $x = 0.13$ . (c)  $E_g = 1.39$  for  $x = 0.33$ . (d)  $E_g = 1.55$  for  $x = 0.5$ . (e)  $E_g = 1.77$  for  $x = 0.65$ .

**E. BAND GAP CALCULATIONS**

CIAS thin films with optimal band gap are used in the application of solar cells. Optical band gap nature either direct or indirect can be determined by the relation (6)

$$\alpha = A(h\nu - E_g)^n / h\nu \tag{6}$$

Where  $h\nu$  is the energy of the photon, 'A', 'h' are the constants,  $E_g$  is the band gap and 'n' is considered to be 1/2 for the indirectly allowed transitions and 2 for the directly allowed transitions. The plot of  $(\alpha h\nu)^2$  versus photon energy ( $h\nu$ ) and linear extrapolation over the photon energy axis determines the band gap. As calculated band gaps for different batch of films of varied Al composition, are shown in the Fig. 11.

**DEVICE FABRICATION**

Solar cell fabrication involved (a) cleaning the stainless steel 10  $\mu\text{m}$  thick substrate, with the detergent followed by in boiling acetone and iso-propanol at 150°C for 15 min each and drying under nitrogen. (b) Molybdenum back contact deposition from the elemental cathode by dc-sputtering to get 450 nm - 500 nm micron continuous thin film (c) Co-sputtering of CIA alloyed thin films of desired stoichiometric

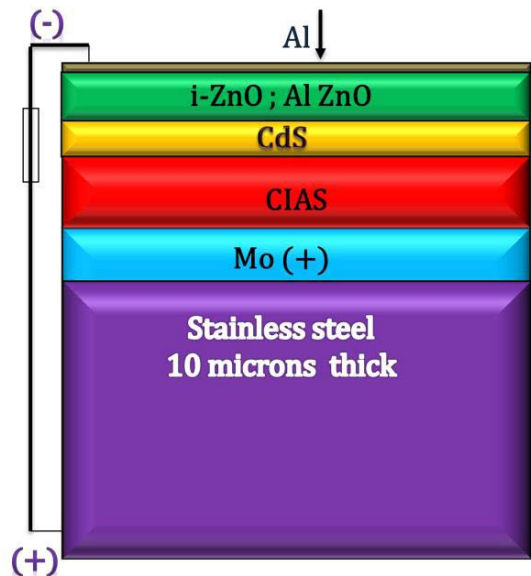


**FIGURE 12.** Schematic cross sectional image of the complete solar cell.

compositions (d) Selenization of co-sputtered thin films to get 1.5  $\mu\text{m}$  – 1.7  $\mu\text{m}$  thick films (e) 50 nm thin films of CdS buffer were deposited by chemical bath deposition

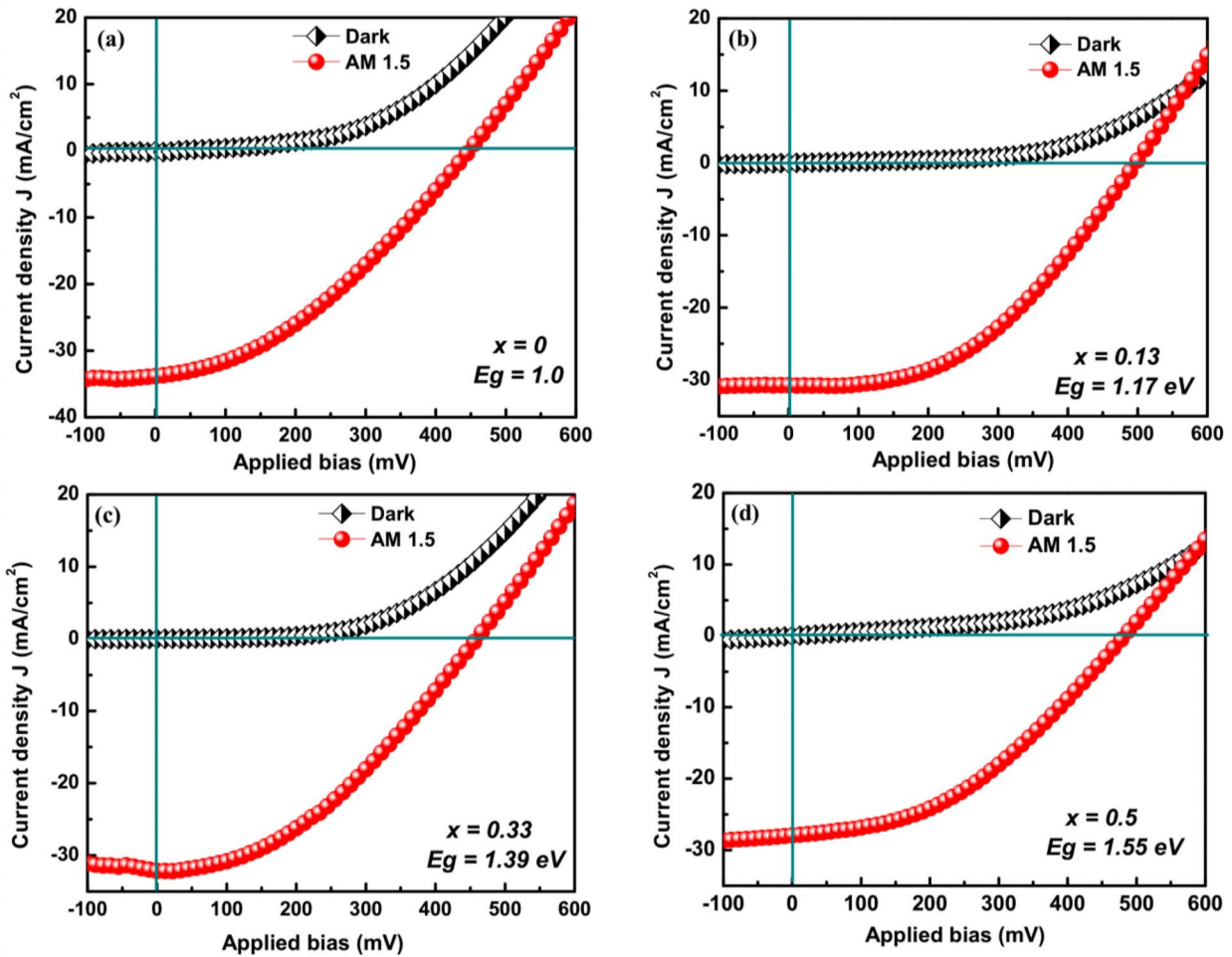


**FIGURE 13.** Current-voltage characteristics of solar cells for various 'x' ratios under dark and A. M. 1.5 G solar illumination. (a)  $x = 0$ . (b)  $x = 0.13$ . (c)  $x = 0.33$ . (d)  $x = 0.5$ .

**TABLE 1.** Variation of solar cell parameters as a function of 'x' ratios.

$\frac{x}{Al+In}$	$E_g$ (eV)	$V_{oc}$ (V)	$I_{Sc}$	$J_{Sc}$	$I_{max}$ (A)	$V_{max}$ (V)	$P_{max}$ (mW)	$FF$	$\eta$ (%)	R at $V_{oc}$	R at $I_{Sc}$	Power (W)
$x=0$	1.0	0.447	0.501	33.52	0.329	0.248	82.03	36.48	5.46	0.51	5.87	0.145
$x=0.13$	1.17	0.496	0.46	30.71	0.348	0.293	102.42	44.73	6.82	0.48	34.3	0.166
$x=0.33$	1.39	0.458	0.475	31.72	0.333	0.255	85.22	39.05	5.68	0.53	22.5	0.147
$x=0.55$	1.55	0.48	0.417	27.83	0.297	0.276	82.07	40.77	5.47	0.60	6.79	0.1377

(f) Bilayer of transparent conducting oxides (iZnO by Rf-sputtering from ZnO target and Al 2% doped ZnO by co-sputtering from Al and Zn cathodes) to get  $\sim 300$  nm thin film. (g) Thermal evaporation of 100 nm grid pattern of Al top contact. Schematic overall finished solar cell was shown in Fig. 12.

## F. DEVICE CHARACTERIZATION

Cross sectional scanning electron micrograph showing the independent layer thickness of the complete solar cell was shown in the Fig.14. Solar cells were fabricated for various 'x' ratios of 0, 0.13, 0.33 and 0.5. The open-circuit voltage increased with the 'x' ratio. Fig. 13 shows the  $J$ - $V$  curves



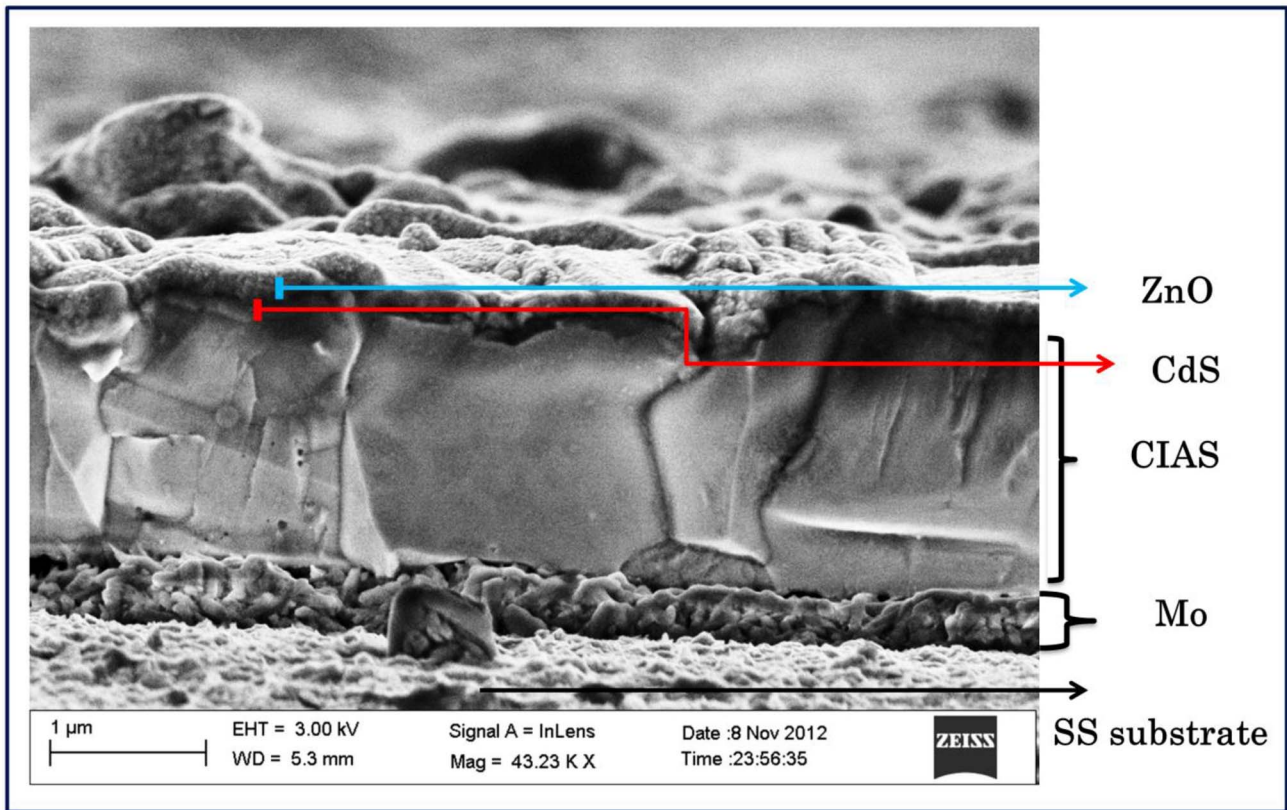


**FIGURE 14.** Cross sectional image of the best solar cell with 6.8% efficiency.

for various Al dopings. Device characteristics of best cell are as follows:  $x = 0.13$ ,  $E_g = 1.17$  eV, fill factor ( $FF$ ) 45.04, Short circuit current density  $J_{sc}$  30 mA/cm<sup>2</sup>.

Solar cell parameters were calculated and tabulated in the Table 1. It was observed that the current density decreased with increase with Al incorporation. Open circuit Voltage  $V_{oc}$  showed an improvement of 50 mV from  $x = 0$  to  $x = 0.13$  and gradually decreased from to 40 mV at  $x = 0.33$  compared to  $x = 0.13$ . In general the increase in  $V_{oc}$  is accompanied by the decrease in  $FF$  and therefore the decrease in efficiency. Similar result was previously reported by Marsillac *et al.* [20]. The lower efficiencies of CIAS solar cells fabricated on stainless steel substrates herein exhibited lower values due to many factors which include: a) Absence of KCN etching and the deposition issues related to CdS deposition. The decrease in the  $V_{oc}$ ,  $J_{sc}$ ,  $FF$  are possibly arise from the Cu<sub>2-x</sub>Se impurity present at the absorber buffer interface. Absence of Cu<sub>2-x</sub>Se phase in XRD pattern may be due to its amorphous nature. It is also to be noted slower KCN etching would sacrifice the fill factor, hence faster KCN etching is preferred. b) Upon increasing Al incorporation, the possibility of Al<sub>2</sub>O<sub>3</sub> formation, cannot be ruled out. Al<sub>2</sub>O<sub>3</sub> is highly resistive phase, showing detrimental effects on the device performance. c) As seen from the XRD pattern, the CIAS absorber films were textured along (204) orientation, which indicated the absence of Na incorporation. In general Na aids the texturing towards (112) preferred

orientation and re-ordering of electrically defect clusters. This would also contribute to the lowering of efficiency of CIAS solar cells, due to the absence of Na incorporation. Currently the various ways to incorporate Na [21] into the absorber is focused in our research group.

### III. CONCLUSION

CIAS thin films were grown on the Mo coated SS substrates, by co-sputtering, followed by the selenization. Two types of selenization of precursor films were studied and the modified selenization gave better results. Adhesion and crystallinity issues are addressed as function of selenium flux. Structural and optical properties of CIAS/Mo/SS were studied in detail. Lattice parameters, decreased and the dislocation density and strain were found to increase, upon (112) peak shifting to higher Bragg's angle, with Al incorporation. Efficiency of the CIAS solar cells can be improved by grading the window layers. CIAS solar cells have been successfully fabricated on flexible substrates CIAS solar cells with better efficiency, are currently focused upon by incorporation of NaF/soda-lime glass thin films (SLGTF) layer between the back contact and the flexible substrate.

### REFERENCES

- [1] Q. Guo *et al.*, "Development of CuInSe<sub>2</sub> nanocrystal and nanoring inks for low-cost solar cells," *Nano Lett.*, vol. 8, no. 9, pp. 2982–2987, 2008.

- [2] A. Jager-Waldau, "Progress in chalcopyrite compound semiconductor research for photovoltaic applications and transfer of results into actual solar cell production," *Solar Energy Mater. Solar Cells*, vol. 95, no. 6, pp. 1509–1517, 2011.
- [3] M. A. Green *et al.*, "Solar cell efficiency tables (version 36)," *Progr. Photovoltaics Res. Appl.*, vol. 18, pp. 346–352, Jun. 2010.
- [4] U. Rau *et al.*, "Electrical characterization of Cu(In,Ga)Se<sub>2</sub> thin-film solar cells and the role of defects for the device performance," *Solar Energy Mater. Solar Cells*, vol. 67, pp. 137–143, Mar. 2001.
- [5] S. Marsillac *et al.*, "High-efficiency solar cells based on Cu(InAl)Se<sub>2</sub> thin films," *Appl. Phys. Lett.*, vol. 81, pp. 1350–1352, Aug. 2002.
- [6] S. H. Wei and A. Zunger, "Band offsets and optical bowings of chalcopyrites and Zn-based II–VI alloys," *J. Appl. Phys.*, vol. 78, no. 6, pp. 3846–3856, 1995.
- [7] R. Aninat *et al.*, "Crystallographic properties and elemental migration in two-stage prepared CuIn<sub>1-x</sub>Al<sub>x</sub>Se<sub>2</sub> thin films for photovoltaic applications," *Journal of Alloys and Compounds*, vol. 566, pp. 180–186, Jul. 2013.
- [8] F. O. Adurođija *et al.*, "Characterization of co-sputtered Cu-In alloy precursors for CuInSe<sub>2</sub> thin films fabrication by close-spaced selenization," *Solar Energy Mater. Solar Cells*, vol. 55, no. 3, pp. 225–236, 1998.
- [9] M. A. Green, "Crystalline and thin-film silicon solar cells: State of the art and future potential," *Solar Energy*, vol. 74, no. 3, pp. 181–192, 2003.
- [10] A. Chirilă *et al.*, "Highly efficient Cu(In,Ga)Se<sub>2</sub> solar cells grown on flexible polymer films," *Nature Mater.*, vol. 10, pp. 857–861, Sep. 2011.
- [11] F. Kessler *et al.*, "Approaches to flexible CIGS thin-film solar cells," *Thin Solid Films*, vol. 480–481, pp. 491–498, Jun. 2005.
- [12] N. R. Baddoo, "Stainless steel in construction: A review of research, applications, challenges and opportunities," *J. Constr. Steel Res.*, vol. 64, no. 11, pp. 1199–1206, 2008.
- [13] B. Murali and S. B. Krupanidhi, "CuIn<sub>1-x</sub>Al<sub>x</sub>Se<sub>2</sub> solar cells fabricated on the flexible substrates by co-sputtering and modified selenization," in *Proc. 2013 IEEE 39th Photovoltaic Specialists Conf. (PVSC)*, Tampa, FL, USA, pp. 2011–2016.
- [14] A. Chirilă *et al.*, "Cu(In,Ga)Se<sub>2</sub> solar cell grown on flexible polymer substrate with efficiency exceeding 17%," *Progr. Photovoltaics Res. Appl.*, vol. 19, no. 5, pp. 560–564, 2011.
- [15] C. S. Barrett and T. B. Massalski, *Structure of Metals: Crystallographic Methods, Principles, and Data*. New York, NY, USA: McGraw-Hill, 1966.
- [16] J. A. Wang *et al.*, "Quantitative determination of titanium lattice defects and solid-state reaction mechanism in iron-doped TiO<sub>2</sub> photocatalysts," *J. Phys. Chem. B*, vol. 105, no. 40, pp. 9692–9698, 2001.
- [17] G. Zoppi *et al.*, "Grain and crystal texture properties of absorber layers in MOCVD-grown CdTe/CdS solar cells," *Semicond. Sci. Technol.*, vol. 21, no. 6, p. 763, 2006.
- [18] B. Murali and S. B. Krupanidhi, "Transport properties of CuIn<sub>1-x</sub>Al<sub>x</sub>Se<sub>2</sub>/AZnO heterostructure for low cost thin film photovoltaics," *Dalton Trans.*, vol. 43, no. 5, pp. 1974–1983, 2014.
- [19] Y. B. K. Reddy *et al.*, "Growth and characterization of CuIn<sub>1-x</sub>Al<sub>x</sub>Se<sub>2</sub> thin films deposited by co-evaporation," *J. Phys. D Appl. Phys.*, vol. 39, no. 24, p. 5124, 2006.
- [20] P. D. Paulson *et al.*, "CuIn<sub>1-x</sub>Al<sub>x</sub>Se<sub>2</sub> thin films and solar cells," *J. Appl. Phys.*, vol. 91, pp. 10153–10156, May 2002.
- [21] R. Wuerz *et al.*, "Alternative sodium sources for Cu(In,Ga)Se<sub>2</sub> thin-film solar cells on flexible substrates," *Thin Solid Films*, vol. 519, pp. 7268–7271, Aug. 2011.



**MURALI BANAVOTH** received the bachelor's degree from Sr. Vijaya Sai Degree College, Osmania University, Hyderabad, India, and the master's degree from the University of Hyderabad, Hyderabad. From 2008 to 2013, he was involved in research for his Ph.D. project on the earth abundant alternate materials for thin-film photovoltaics. He was the recipient of several awards and honors, including the Prathibha Puraskar Award for Excellence in his bachelor's education, the Junior and Senior Research Fellows of the

Council of Scientific and Industrial Research in India. His current research interests include the field of inorganic–organic quantum dots/nanostructured-based bulk heterojunction/hybrid solar cells and photo detection, nano particle ink-based solar cells and photodetection, development of Cu-based chalcogenide/chalcopyrite [Cu<sub>2</sub>ZnSnS<sub>4</sub>, Cu<sub>2</sub>ZnSnSe<sub>4</sub>, Cu<sub>2</sub>CoSnS<sub>4</sub>, Cu(In,Ga)Se<sub>2</sub>, Cu(In,Al)Se<sub>2</sub>, Cu<sub>3</sub>BiS<sub>3</sub>] inorganic thin-film/nanostructured photovoltaics and photodetection, transparent conducting oxides and alternate buffers for thin-film solar cells, and the utilization of graphene quantum dots for low-cost photovoltaics. He is currently a Research Associate with Materials Research Centre, Indian Institute of Science, Bangalore, India, under the supervision of Prof. S. B. Krupanidhi.



**M. MADHURI** received the Diploma and the B.E. degrees in mechatronic engineering from Visvesvaraya Technological University, Belgaum, India, and Don Bosco Institute of Technology, Bangalore, India, in 2009 and 2012, respectively. Her current research interests include solar panel tracking systems. Her current position is to assist the project based on the fabrication of the thin-film solar cells and to characterize the solar cells at Materials Research Centre, Indian Institute of Science, Bangalore, India, under the supervision of Prof. S. B. Krupanidhi.



**S. B. KRUPANIDHI** received the Ph.D. degree in solid state physics from Delhi University, New Delhi, India, in 1981, and held post-doctoral positions at Queen's University, Kingston, ON, Canada, until 1984. He was a Professor at Pennsylvania State University, State College, PA, USA, and also a Principal Scientist at Motorola, Albuquerque, NM, USA, until 1988. Since 1995, he has been a member of the faculty at MRC. He was the recipient of several awards and honors, including the Two Engineering Invention Awards

at Motorola, in 1986, the MRSI Medal, India, in 1997, the Fellow of Indian Academy of Sciences, in 2003, the VASVIK Medal, in 2004, the MRS Superconductivity-Materials Science Award, in 2004, the Tatachem Chair Professor, Indian Institute of Science, Bangalore, India, in 2006, and the Rustum Choksi Medal for Research Excellence, in 2006. He has been selected for J. C. Bose National Fellowship for the year 2008, constituted by the Department of Science and Technology, India. He is a fellow of the Indian Academy of Sciences and the Indian National Science Academy and Engineering. His current research interests include the growth of low dimensional III–V and III–Nitride semiconductor hetero-structures for high brightness LEDs and infra-red detection involving techniques such as molecular beam epitaxy, metal-organic chemical vapor deposition, and multicomponent functional oxide thin films deposited by multimagnetron reactive sputtering, ECR plasma-assisted growth, excimer laser ablation, and sol-gel technique, low energy ion induced effects in multi-component oxide films, epitaxy and ion-surface interactions, ferroelectrics and dielectrics for random access memory applications, artificial superlattices of ferroelectric and dielectrics for tunable microwave device application, studying the coupled dynamics of electrical and magnetic domains in artificial superlattices of multiferroics and dielectrics, and synthesis and characterization of perovskite nanostructures using physical and chemical techniques.